Ceramics International 49 (2023) 11579–11588

Contents lists available at ScienceDirect

Ceramics International

journal homepage: www.elsevier.com/locate/ceramint

Integration of conductive silver sensors on zirconia ceramics by screen-printing for monitoring strain under applied load

Junhui Zhang [a,b], Maziar Ahmadi [a,b], Marc Serra [a,b], Emilio Jimenez-Pique [a,b], Luis Llanes [a,b,*], Gemma Fargas [a,b,**]

[a] CIEFMA – Department of Materials Science and Engineering, EEBE, Universitat Politècnica de Catalunya – BarcelonaTech, Barcelona, 08019, Spain
[b] Barcelona Research Center in Multiscale Science and Engineering, Universitat Politècnica de Catalunya – BarcelonaTech, Barcelona, 08019, Spain

ARTICLE INFO

Keywords:
Conductive silver ink
Zirconia
Sensors
Strain monitoring

ABSTRACT

There is a growing interest in zirconia ceramics due to their high flexural strength, excellent corrosion resistance and good biocompatibility. The assembly of advanced zirconia material with functions of sensing, actuation and controlling to solve the problems that may arise during its use is critical to ensure long-term service and performance. Within this context, the objective of this work is to analyse the structural health of zirconia samples by screen-printing silver-based conductive ink on the surface subjected to maximum load under flexural testing. In doing so, silver conductive ink was formulated using silver nanoparticles where polyvinyl pyrrolidone acted as the capping agent. Silver ink was then screen-printed onto zirconia samples and sintered at 200 °C. The resistance of the sensors was measured and the sensing capabilities of printed conductive patterns were investigated using the four-point probe method. Experimental findings displayed a reproducible direct correlation between electrical resistance change and strain resulting from surface displacement under applied load in four-point bending.

1. Introduction

Ceramic materials based on zirconia (ZrO_2) are becoming increasingly attractive as structural components, thermal barrier coatings, solid oxide fuel cells and smart implants due to their unique high mechanical strength and fracture toughness, excellent corrosion resistance, good biocompatibility, and elevated ionic conductivity [1–3]. Zirconia is an oxide ceramic material with special crystal structure transition characteristics, i.e. phase transformation from tetragonal to monoclinic (t→m) during cooling results in residual compressive stresses and micro-cracks [4]. To avoid this, zirconia is stabilized by the addition of rare earth elements. Yttria (Y_2O_3) is the most commonly used additive to stabilize the tetragonal or cubic phase at room temperature, depending on the amount of dopant [5]. The microstructure and properties also change markedly with yttria content. Polycrystalline tetragonal zirconia doped with 3 mol.% yttria (3Y–ZrO_2) has been used as dental implants and prostheses due to its outstanding mechanical properties [6]. Meanwhile, the 8 mol.% Y_2O_3 stabilized cubic zirconia (8Y–ZrO_2) has been widely used as solid oxide fuel cells, sensors and catalysis supports because of its high ionic conductivity, thermal and chemical stability [7–9].

Measurement of different parameters such as force and displacement, or corresponding stress and strain, is one of the most important necessities in engineering. In this regard, strain [10], pressure [11], bio- [12] and hybrid [13] sensors have been produced and used. Sensors could convert physical or chemical parameters like force, humidity, and light into an electrical output. As sensors have a decisive effect on quantity and quality, great care has been taken in their production. Among different modern manufacturing processes, screen printing has proved its possibility with great potential for the fabrication of sensors and electronic components [14]. Screen printing is the process that transfers the ink pass through the patterned stencil with a squeegee, leading to a printed pattern. It is often considered to print conductive inks onto various rigid or flexible substrates because it is a simple, cost-effective and fast method [15]. Conductive inks for the screen

* Corresponding author. CIEFMA – Department of Materials Science and Engineering, EEBE, Universitat Politècnica de Catalunya – BarcelonaTech, Barcelona, 08019, Spain.
** Corresponding author. CIEFMA – Department of Materials Science and Engineering, EEBE, Universitat Politècnica de Catalunya – BarcelonaTech, Barcelona, 08019, Spain.
E-mail addresses: luis.miguel.llanes@upc.edu (L. Llanes), gemma.fargas@upc.edu (G. Fargas).

https://doi.org/10.1016/j.ceramint.2022.12.005
Received 8 September 2022; Received in revised form 18 November 2022; Accepted 1 December 2022
Available online 5 December 2022

printing process contain nanomaterials such as metallic nanoparticles [16,17], carbon nanomaterials [18] and conductive polymers [19]. Among them, silver (metallic) nanoparticles (Ag NPs) have attracted considerable research interest due to their high electrical conductivity, low cost as compared to gold, relative resistance to oxidation, and biocidal properties [20–22]. Currently, silver-based inks are used in micro- or nano-electronic industries aiming to a broad set of applications such as sensors [23–25], solar cells [26,27], thin-film transistors [28] or supercapacitors [29,30].

Advanced zirconia material incorporates functions of sensing, actuation, and controlling to describe and analyse a situation as well as to make decisions based on the available data in a predictive or adaptive manner, thereby performing smart actions [31,32]. Since zirconia is a brittle material with significant sensitivity to surface defects, good quality control is necessary to enhance its long-term performance. With advanced printing technologies, it is possible to print materials on zirconia substrates, with the ability to sense surface displacement, temperature, or PH. In this regard, Moura et al. [31] printed silver-based wires in zirconia substrates using laser technology for smart implant applications. Silver-based wires with good quality and a resistivity of 10^{-7} Ω m were achieved, being a conductor path to the electrical flow. However, the flexural strength of zirconia decreased as the laser passage was performed. Furthermore, the sensing capability of the sensor was not investigated.

Moreover, zirconia ceramics show high thermal, chemical and mechanical stability, which makes them very suitable potential candidates for sensor applications. Materials such as alumina and zirconia have been developed as sensing surfaces [33–35]. Hrovat et al. [36] reported thick-film resistors on zirconia substrates for strain gauge applications. They concluded that the sensing elements on zirconia substrate exhibited improved characteristics when compared with alumina. To the authors' knowledge, there is no research work in the literature reporting the integration of sensors on zirconia substrate by screen-printing silver conductive ink. This is particularly true regarding studies addressing the relationship between measured electrical resistance of silver conductive ink and surface displacements resulting from applied load in zirconia. This may be quite useful for studying crack imitation and propagation of zirconia material. Structural health monitoring of zirconia material is key to ensure long-term service and performance of corresponding components.

Following the above ideas, this work addresses the ability of screen-printing silver-based ink on zirconia substrates, by evaluation of the electrical response of silver conductive ink when load is applied. The aim is to improve the knowledge of the design of strain sensors on zirconia substrate, with particular attention to the relationship between surface displacement and measured electrical resistance. In the current study, the conductive ink was formulated using silver nanoparticles where polyvinyl pyrrolidone acted as the capping agent. Silver ink was then screen-printed on zirconia substrates and thermally sintered. A systematic investigation, including crystal structure, microstructure, roughness, and resistivity of screen-printed silver patterns has been performed. Moreover, the sensing capabilities of printed conductive patterns were investigated when the specimen surface was subjected to flexure under four-point bending. Results were compared with those measured on samples where a commercial ink was used.

2. Materials and methods

2.1. Materials

Silver nanoparticles and zirconia powders stabilized with 3 mol.% yttria (3Y–ZrO_2) were supplied by Nano Technology Inc. (Korea) and Tosoh-Zirconia (TZ-3YSB-E, Tosoh, Japan) respectively. Glycerol ($C_3H_8O_3$, 99.5%) and polyvinyl pyrrolidone (PVP, Mw ~ 40,000) were provided by Sigma-Aldrich. Polyester resin was supplied by Euroresins Ltd. (FS9900/AC SIRESTER, Spain). Commercial silver nanoparticle ink for screen printing was purchased from Sigma-Aldrich (Product No. 901090). All chemicals were used as-received, without further purification.

2.2. Formulation of silver ink and screen printing

Silver conductive ink was prepared by dispersing as-received silver nanoparticles into glycerol, where polyvinyl pyrrolidone (PVP) and polyester acted as the capping agent and the binder respectively. The mixture was homogenized using a dual asymmetric centrifugal mixer (SpeedMixer, DAC a50.1 FVZ-k) for 5 min. Typically, silver ink consisted of 51 wt% Ag NPs, 43 wt% glycerol, 2.6 wt% PVP and 3.4 wt% polyester resin. Silver conductive ink was screen-printed on zirconia substrate. The printing process was performed on an automatic screen printer (Upart Equipment Ltd., China) using a nylon mesh (62T mesh count). As-printed patterns were dried at 60 °C for 45 min and sintered at 200 °C for 45 min in an oven (Digitheat-TFT SELECTA). Fig. 1 shows the schematic representation of the general procedure. A copper wire was then attached to Ag patterns using a silver-epoxy adhesive (Atom Adhesives, AA-BOND 918-10 gm-Syr), as measurement lead.

Samples fabricated using commercial silver ink were also produced to compare with the as-prepared ones. In this regard, conductive silver patterns were screen-printed using a polyester mesh (140T mesh count), following the same sintering process as mentioned above.

2.3. Preparation of zirconia substrates

Zirconia bars of 50 × 8 × 3 mm^3 were uniaxially pressed at 50 MPa and then cold isostatic pressed (CIP) at 300 MPa. As-pressed samples were pressureless sintered. During sintering, the de-binding process was carried out at 700 °C for 1 h, and the sintering process at 1450 °C for 2 h, using a furnace (Nabertherm, Germany). Heating and cooling rates were 3 °C/min. Prior to use, the zirconia substrates were polished using suspensions of diamond particles down to 1 μm, cleaned with acetone and ethanol, and dried at room temperature.

2.4. Characterization

Characterization of Ag NPs as well as of zirconia microstructure was carried out by means of field emission scanning electron microscopy (FESEM, Carl Zeiss Neon 40, Oberkochen, Germany) using a unit equipped with energy dispersive X-ray spectroscopy (EDX).

Crystalline phases were determined by X-ray diffraction (XRD, Bruker D8 Advance Diffractometer, USA), using Cu K_α radiation (40 kV and 40 mA) in the 2θ range from 20 to 90° with an angular step of 0.01° at 1 s per step.

The thickness of the printed patterns was determined by focus ion beam/scanning electron microscopy (FIB/SEM), employing the unit referred above.

Topographic images and surface roughness of printed silver patterns, including root-mean-square (Rq) and average roughness (Ra), were obtained by atomic force microscopy (AFM, Veeco Dimension 3100), which has maximum lateral (x, y) and vertical (z) scan ranges of 90 μm and 6 μm respectively. Images were obtained over an area of 15 μm × 15 μm with 512 points per scan line and 512 scan lines.

Scratch tests were carried out using a nanoindentation unit (Nanoindenter XP, MTS) with a Berkovich diamond tip, under sliding contact conditions. For as-prepared ink, applied load was increased up to 150 mN, over a scratch length of 500 μm and following a lateral displacement rate of 10 μm/s. For commercial ink, similar scratch length and displacement rate were used, but up to a maximum load of 25 mN. The cross-sectional morphology of the scratch was examined by FIB/SEM after testing, to evaluate the interface delamination of the film stack around scratch tracks.

The sheet electrical resistance of printed patterns was measured using the four-point probe resistance tester (Ossila Four-Point Probe

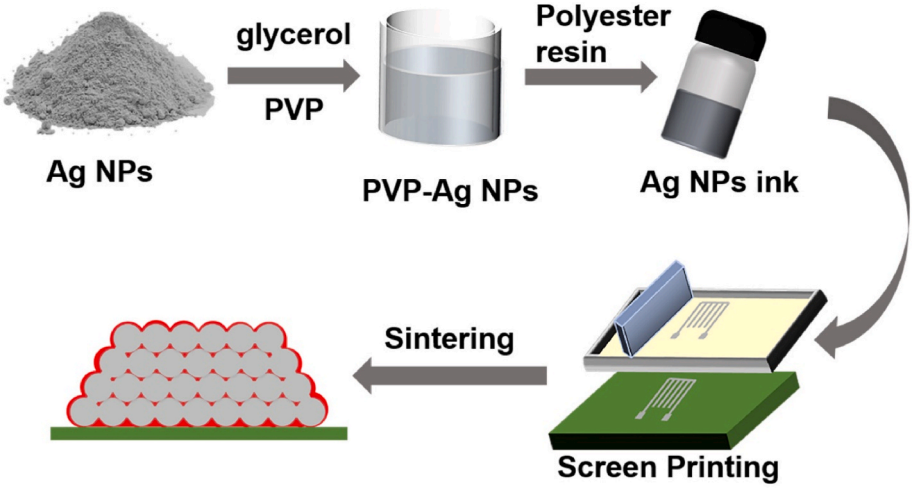

Fig. 1. Schematic illustration of the whole process of screen-printing silver conductive ink: from the formulation to the sintering process of conductive patterns.

System, Ossila Ltd.). On each sample, 5 points were measured and averaged. The sheet resistance is calculated by the following formula [37]:

$$Rs = CF \times V/I \quad (1)$$

where Rs is the sheet resistance, CF is a geometrical correction factor, assumed to be 3.40 for as-prepared ink and 1.45 for commercial ink, V is the voltage between the inner probers and I is the applied current. Electrical resistivity was then calculated from the measured sheet resistance and film thickness using the following equation [38]:

$$\rho = Rs \times t \quad (2)$$

where ρ is the resistivity, Rs is the sheet resistance of the film, and t is the average thickness of the film.

Resistance of the sensors was measured, using a digiltal multimeter (Keithley 2700), as specimens were tested under load control in flexion. In doing so, testing was conducted using a four-point bending fully articulated test jig with inner and outer spans of 20 and 40 mm, respectively. Flexural strength tests were performed on an Instron 8511 servohydraulic machine. Load was progressively increased in 50 N intervals with intermediate holding steps of 30s, until failure of the tested specimen. All the experimental data were simultaneously recorded in real-time.

A representative as-printed specimen for flexural testing is shown in Fig. 2. Here, sensor is shown to consist of a single rectangular strip of conductive ink, aligned with the specimen length. For all the sensors, the conductive stripe had a nominal length of 32 mm, i.e. within the 40 mm outer span of the four-point bending testing fixture used. A copper wire was then attached to Ag patterns, using a silver-epoxy adhesive, as measurement lead. It should be noticed that consideration of printing resolution as experimental variable was out of the scope of this study. Nevertheless, taking into account that it is indeed a critical parameter to be optimized if sensor integration and performance want to be enhanced [16], the need of a more systematic study addressing printing resolution of the ink used is highlighted for future work.

The sensitivity of the sensor can be determined by calculating the gauge factor (GF), which is defined as the ratio of change of resistance, $\Delta R/R_0$, to the strain and is represented as [39]:

$$GF = (\Delta R / R_0) / \varepsilon \quad (3)$$

where $\Delta R/R_0$ is the relative change in resistance, and ε is the elastic strain resulting from applied stress. The GF was calculated from the slope of the best-fit linear regression of the data.

3. Results and discussion

3.1. Characterization of Ag NPs

Morphological structure and size of Ag NPs have important effects on the electrical, optical, and sensing properties. Fig. 3 (a) displays FESEM images of Ag NPs, indicating that they are spherical in shape. It can be also observed that larger particles of Ag NPs were formed due to the aggregation of nanoparticles during the synthesis process. A particle size distribution histogram determined from FESEM images showed that average size of Ag NPs was around 160 nm, Fig. 3 (b). The elemental composition of the Ag NPs was analyzed by means of EDX, as shown in Fig. 3 (c). A sharp signal was observed at 3 keV, which was typical for the absorption of metallic silver nanoparticles [40,41]. No other obvious impurity peaks were detected, indicating the high purity of Ag NPs.

3.2. Characterization of screen-printed Ag patterns

3.2.1. X-ray diffraction (XRD) analysis

XRD analysis was performed for Ag NPs, as well as Ag films prepared by as-prepared and commercial inks. Results are given in Fig. 4. All the diffractograms showed typical peaks at 2θ values of around 38.1°, 44.3°, 64.4°, 77.4°, and 81.5°, corresponding to (111), (200), (220), (311) and (222), respectively. These patterns exhibited the face-centered cubic

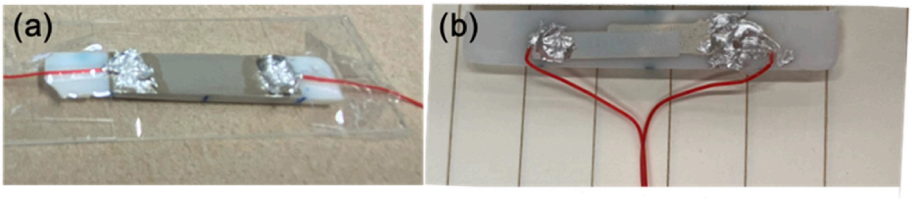

Fig. 2. Representative as-printed specimens for flexural testing: (a) as-prepared ink, and (b) commercial ink.

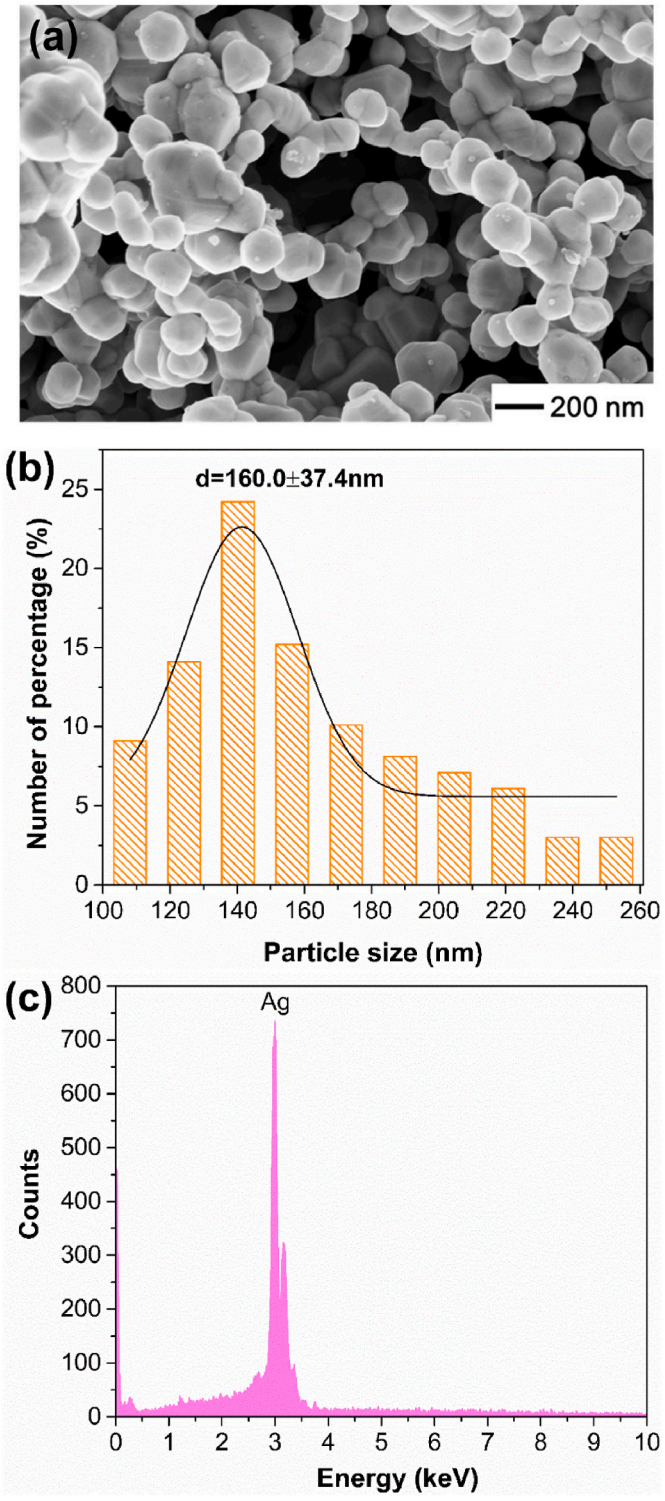

Fig. 3. Characterization of Ag NPs: (a) FESEM micrographs; (b) Particle size distribution histogram from the FESEM image; and (c) Energy-dispersive X-ray spectrum.

(FCC) structure of silver which correlated to those of the Joint Committee on Powder Diffraction Standards (JCPDS file no. 04–0783) [42,43]. The high intense peak in the XRD pattern indexed as (111) suggested a preferential growth of nanoparticles [44]. No other diffraction peaks in Ag NPs can be found in Fig. 4 (a), indicating the purity of the Ag NPs. That was consistent with FESEM results, as shown in section 3.1. Meanwhile, new phases were not evidenced, after printing and

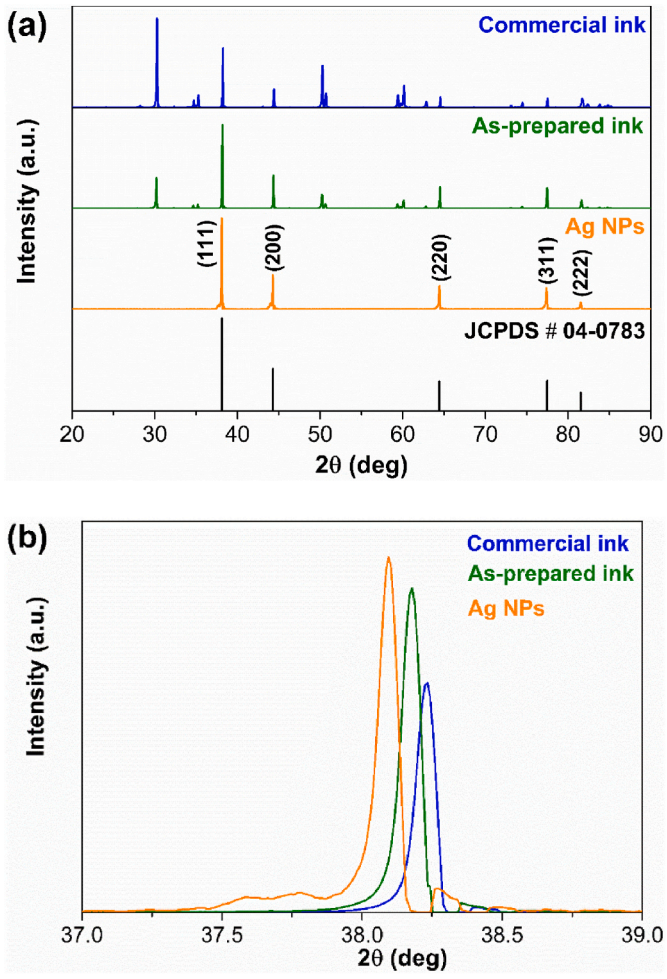

Fig. 4. (a) XRD patterns of Ag NPs and screen-printed Ag films along with standard silver patterns, and (b) magnification of the (111) peak.

sintering, for Ag films prepared with as-prepared ink and commercial ink. Other peaks in Ag films prepared from as-prepared and commercial inks may be described as contributions from zirconia substrates [45].

Fig. 4 (b) shows the detailed scan of the most intense peak (111). It was rather broader than the one observed for printed Ag films, indicating a smaller crystallite size. Bragg's law was used to calculate the lattice parameter, while Debye-Scherrer's formula was employed to measure the crystallite size of Ag NPs., as given below [46]:

$$D = K\lambda/\beta\, Cos\, \theta \quad (4)$$

where D is the crystallite size of Ag NPs, K is a constant related to crystallite, normally taken as 0.94 for spherical crystals with cubic symmetry, λ is the wavelength of the X-ray source (0.15417 nm) used in XRD, β is the full width at half maximum (FWHM) of the diffraction peak in radian, and θ is the Bragg's angle in degrees.

As shown in Table 1, based on the crystal plane corresponding to the

Table 1
Lattice parameters and crystallite sizes of Ag NPs and screen-printed Ag films.

Sample	Peak 2θ	FWHM β	Miller indices	Lattice constant (nm)	Crystallite size (nm)
Ag NPs	38.1	0.143	(111)	0.236	86
As-prepared ink	38.2	0.080	(111)	0.236	109
Commercial ink	38.2	0.078	(111)	0.236	112

highest peak (111), the lattice constant of Ag NPs was 0.236 nm and the crystalline size of Ag NPs was 86 nm. It is noted that grain growth of Ag NPs has been observed when the printed films were sintered at 200 °C, due to aggregative growth [47,48].

3.2.2. Field-emission scanning electron microscopy (FESEM) and energy-dispersive X-ray analysis (EDX)

As-printed Ag patterns using two types of inks strike a clear stance through morphological properties, where the microstructures are quite different in terms of particle morphology, size and degree of contact. As seen in Fig. 5 (a1, a2, b1, b2), both annealed films were fairly smooth and uniform on the zirconia substrate. Densely packed Ag nanoparticles are evidenced in the low magnification images shown in Fig. 5 (a1, b1). Adjacent particles connect to form network structures. Compared with Ag film from commercial ink, the Ag film derived from as-prepared ink showed an irregular crystal structure, consisting of small and large particles and exhibiting a loose surface morphology. Compactly interconnected particles for both Ag films; and thus, forming an easy pathway for the transportation of electrons, are seen in the high magnification FESEM images shown in Fig. 5 (a2, b2). However, the Ag film from the as-prepared ink shows some nanoparticles' aggregates, yielding then a rougher surface (Section 3.2.4); and thus, lower conductivity values [49] (Section 3.2.6).

The chemical composition of the films derived from both inks was identified by EDX spectra, as seen in Fig. 5 (a3, b3). A strong characteristic peak of Ag appears in both EDX spectrums, demonstrating that the nanoparticles observed in FESEM images (Fig. 6 a1, a2, b1, b2) were composed of silver [50]. Furthermore, two elements (carbon and oxygen) for as-prepared Ag ink were detected, which was in accordance with the original chemical composition of the compounds. The annealed sample contained mainly silver phases. Carbon and oxygen elements might be contributed from solvent (glycerol), binder (polyester resin), and capping agent (PVP). Moreover, most of the compounds were still left in the film after annealing at 200 °C. This was the reason for the film from as-prepared ink to have a lower Ag content and higher organic residue. The higher silver content from commercial ink can increase the conductivity. Meanwhile, Zr signal was also observed in EDX results corresponding to Ag film printed using the commercial ink, Fig. 5 (a3), possibly because its smaller thickness, which allows then the electron beam to penetrate through it until the substrate [51].

3.2.3. Focused ion beam (FIB) analysis

The FIB cross-sectional images of Ag films using the two types of inks are shown in Fig. 6. Cracks are absent in both films. Moreover, this figure clearly shows the defined interface between the film and the zirconia substrate. However, as mentioned before, the microstructural characteristics of Ag films using the two types of inks were different, which were dependent on the solvent evaporation rate and thermal decomposition of silver ink. The presence of voids in both Ag films was mainly due to the quick evaporation of low boiling point liquids present in Ag ink after the annealing process [52,53]. The as-prepared ink was derived from glycerol in a solvent, as glycerol has a higher boiling point of 290 °C. Hence, most of the solvent was still left in the film, surrounding the silver particles, preventing their connection with each other and resulting in a rough morphology [54]. The cross-sectional thicknesses of Ag films for as-prepared and commercial inks were around 12 μm and 1.2 μm, respectively. The thickness obtained is later used to determine bulk resistivity [55].

3.2.4. Atomic force microscopy (AFM) analysis

The surface morphology, as well as the roughness of printed silver patterns, were measured by AFM. Fig. 7 shows two and three dimensional topographic scans of the films. Each scan represented a 15 μm × 15 μm lateral area. The film from as-prepared ink had bulges. It was different from the surface using commercial ink, which contained islands. Average surface roughness, Ra, and root-mean-square one, Rq, were 382 and 495 nm, respectively, for the as-printed ink. Meanwhile, the commercial film had Ra and Rq values of 53 nm and 68 nm, respectively. The as-prepared silver ink showed coarser silver grains and increased surface roughness compared to commercial ink, which was consistent with FESEM images in Section 3.2.2 and Section 3.2.3.

3.2.5. Scratch test

A quantitative assessment of the adhesion properties of thin films is important to guarantee not only the reliability of the screen-printed film but also the performance of the sensor system. In this regard, scratch tests were carried out to determine the damage mechanism and critical loads of Ag films. Fig. 8 shows FESEM images of the resulting scratch tracks. Critical load L_c at which the Ag film from as-prepared ink failed was 73 mN. It is almost three times higher than that assessed for the Ag film from commercial ink, i.e. 20 mN. The measured higher load-bearing capability should be partly linked to the higher thickness exhibited by the former [56]. Nevertheless, there are several other factors that might affect adhesion, such as surface energy, polarities of the joined surfaces, solvent residues in the inks, or absorption of solvents into substrate surfaces [37]. Accordingly, differences in adhesion between commercial

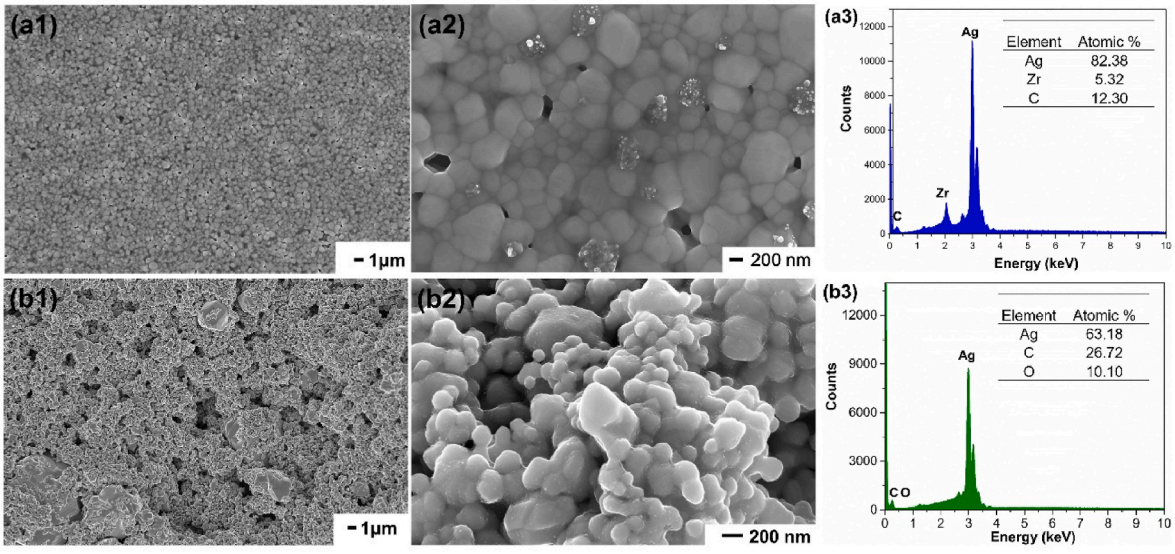

Fig. 5. FESEM images and EDX spectra of Ag patterns printed on zirconia substrate: (a1-a3) with commercial ink, and (b1-b3) with as-prepared Ag ink.

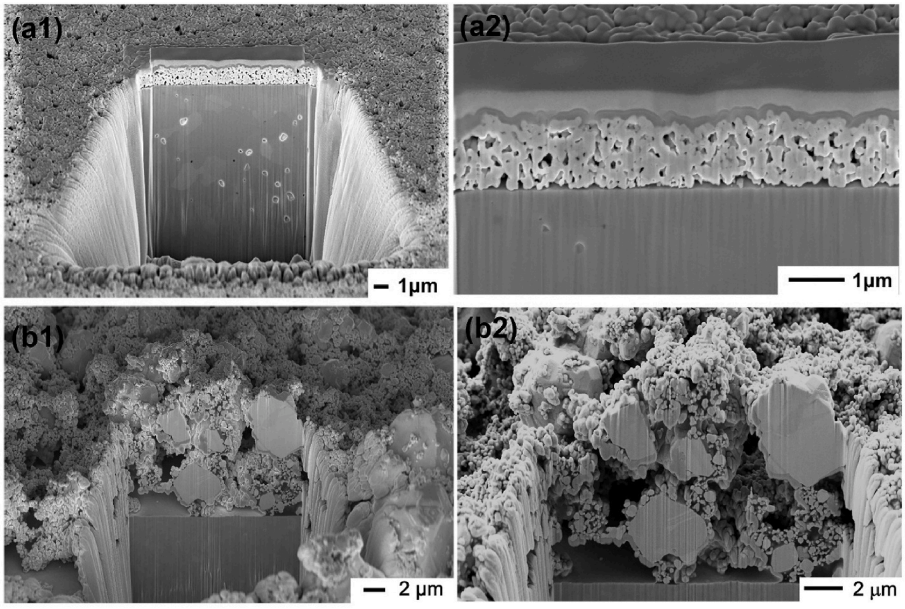

Fig. 6. FIB cross-sectional images of Ag patterns on zirconia substrate: (a1, a2) with commercial ink, and (b1, b2) with as-prepared Ag ink.

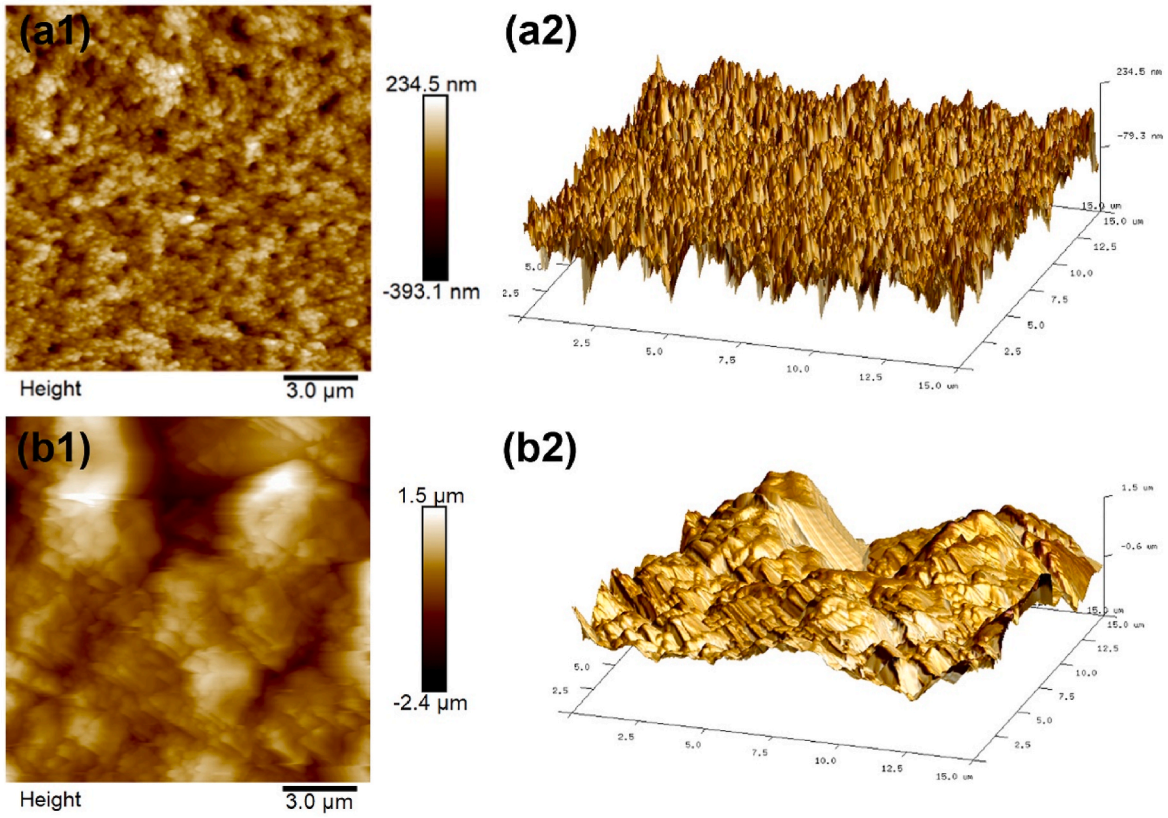

Fig. 7. 2D and 3D topography images of the printed silver patterns: (a1, a2) with commercial ink, and (b1, b2) with as-prepared silver ink.

and as-prepared inks could also be related to the distinct chemical nature of polymers in these inks, as reported by Hicks et al. [57].

Below the critical load in the scratch tests, films were ploughed by the indenter tip resulting in plastic deformation and cracking, Fig. 8 (a2, b2). On the other hand, as critical load is reached, there is a transition in the damage scenario into one characterized by delamination or buckling of the film. Further increase in applied load, finally yields breakdown of film through cracking along its thickness, Fig. 8 (a4, b4).

3.2.6. *Sheet and bulk resistivity of screen-printed Ag patterns*

Sheet resistance was measured using the four-point probe technique, and the corresponding resistivity was calculated by using equation (2). Electrical properties measured are summarized in Table 2. The resistivity of the film from the as-prepared ink was about 5.4×10^{-6} Ω m.

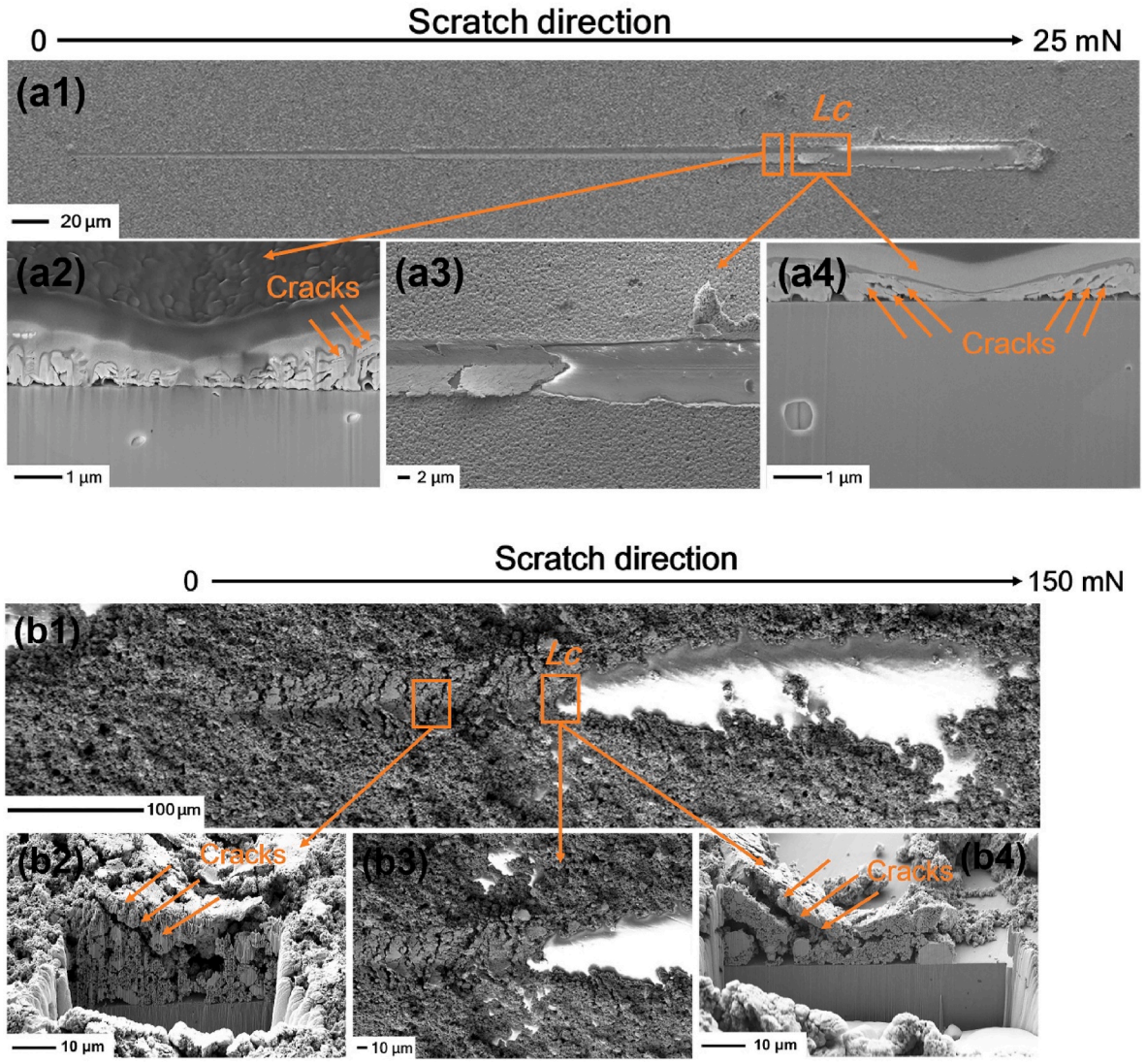

Fig. 8. FESEM images of scratch tracks, and critical load measured for different Ag patterns: (a1-a4) with commercial ink, and (b1-b4) with as-prepared Ag ink.

Table 2
Sheet resistance/conductivity measured for printed Ag patterns on zirconia substrate.

Sample	Thickness (μm)	Sheet resistance (Ω/□)	Resistivity (Ω·m)	Conductivity (S/m)
As-prepared ink	12	0.45	5.4×10^{-6}	1.9×10^{5}
Commercial ink	1.2	0.03	3.4×10^{-8}	2.9×10^{7}

This value is similar to the one reported by Hyun et al. [16], 5.5×10^{-6} Ω m, for screen-printed silver ink (77 wt %) on polyimide film. Direct comparison of the conductivity values for commercial and as-prepared inks indicates that it is higher (about two orders of magnitude) in the film derived from the former. That outcome was expected, since the latter exhibits aggregates of particles with rough morphology as well as coarse silver grains (higher surface roughness), besides impurities and porosity resulting from the sintering process, which may hamper the mean free path of electrons, yielding then a lower conductivity. A denser microstructure would increase the electrical conductivity, which indicates that enhanced densification in the sintering process is key to attain optimal electrical properties [31,52].

3.2.7. *Electromechanical performance of the printed sensors*

Four-point bending tests with simultaneous measurements of electrical resistance and applied load were performed (Fig. 9). Experimental data is plotted in terms of electrical resistance – strain in Fig. 10, aiming to analyse sensing capabilities of printed conductive patterns under bending conditions. In doing so, strain experienced by the zirconia specimen at the surface subjected to maximum stress was calculated assuming linear stress-strain response for the tested specimen up to failure, and using a Young modulus value of 210 GPa for zirconia. A direct correlation between relative changes in electrical resistance and strain is found. It may be physically rationalized by the corresponding increase of the inter-filler distance as well as cracking phenomena in the screen-printed network [37]. GF was calculated from linear regression fitting (coefficients of determination of 0.98), as shown in Fig. 10. Both sensors exhibited good strain sensitivity, with gauge factors of 6 and 5 for as-prepared and commercial inks respectively. These high GF values compare favourably with respect to those typically exhibited by commercial foil strain, i.e. about 2 [58]. In this regard, it should be highlighted that a slightly better sensing capability (higher value of GF) is obtained for the sample with as-prepared ink. Looking into future applications of these sensors in smart implants to monitor their mechanical integrity, it should be noticed that protection of strain gages and their circuits from the effects of bodily fluids is indeed a big challenge [59].

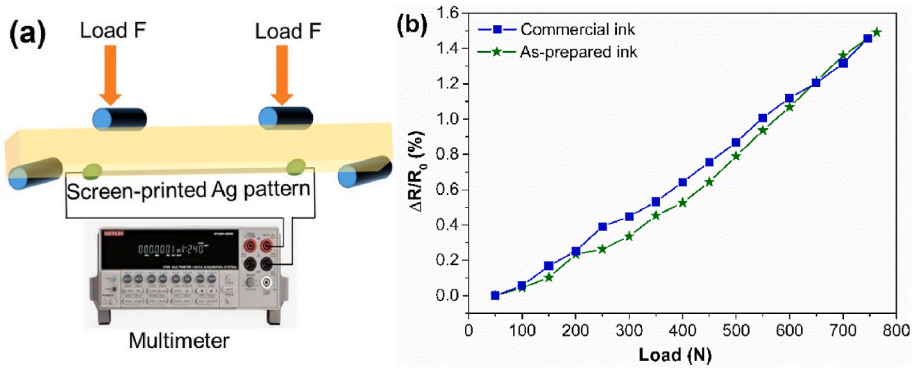

Fig. 9. (a) Schematic of four-point bending test and electrical resistance measurement set-up, and (b) electrical resistance changes as a function of applied load.

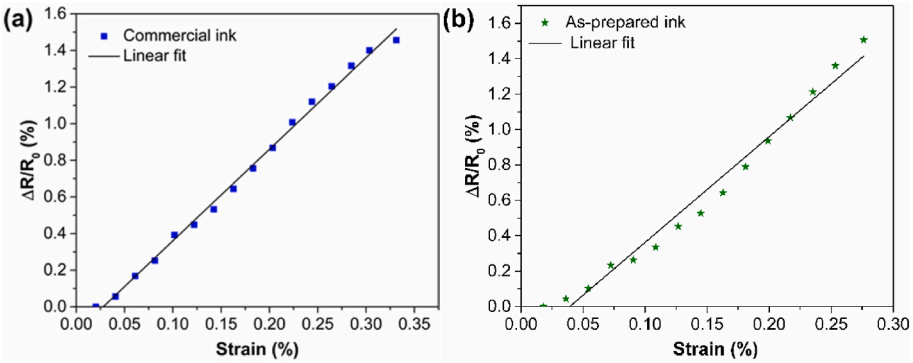

Fig. 10. Electrical resistance changes as a function of strain (resulting from applied stress in the linear elastic regime), and linear regression fitting, for zirconia substrates with silver sensors screen printed using (a) commercial and (b) as-prepared inks.

Within this context, a strategy to overcome this issue could be to design the implant such that strain gages or printed sensors could be inserted (i.e. mounted inside) in the implant itself [60]. Hence, a systematic and in-depth study in this direction is recommended as future research action.

4. Conclusions

Integration of sensors on zirconia substrates has been successfully achieved by screen-printing silver conductive ink directly on the ceramic material, and subsequent heating at 200 °C. The conductive ink was formulated using silver nanoparticles with a diameter of 160 nm at a solid loading of 51 wt%. No phase transformation and formation of new oxides were detected after printing and sintering, as compared to as-received Ag NPs. The resultant Ag films were uniform and showed satisfactory adhesion strength to the zirconia substrate. The printed film exhibited good electrical properties with a resistivity of 5.4×10^{-6} Ω m. Compared to commercial ink, the formulated ink reached equivalent properties for strain monitoring. The promising results obtained for printed lines show that the formulated ink is suitable for electronic application and detection of the structural health of zirconia during its use.

Declaration of competing interest

The authors declare that they have no known competing financial interests or personal relationships that could have appeared to influence the work reported in this paper.

Acknowledgments

This work has been funded in part by the Spanish Ministry of Science, Innovation and Universities and the Agencia Estatal de Investigación through grants PGC2018-096855-B-C41 and PID2021-126614OB-I00. J. Zhang would like to acknowledge China Scholarship Council (CSC) for financial support (No. 201706740094). The authors gratefully acknowledge the assistance of Gema Lopez in the measurement of resistance using four point-probe resistance tester.

References

[1] X. Zhang, X. Wu, J. Shi, Additive manufacturing of zirconia ceramics: a state-of-the-art review, J. Mater. Res. Technol. 9 (2020) 9029–9048, https://doi.org/10.1016/j.jmrt.2020.05.131.
[2] V. Thakare, Progress in synthesis and applications of zirconia, Int. J. Eng. Res. Dev. 5 (2012) 25–28.
[3] C.R.D. Ferreira, A.A.G. Santiago, R.C. Vasconcelos, D.F.F. Paiva, F.Q. Pirih, A. A. Araújo, F.V. Motta, M.R.D. Bomio, Study of microstructural, mechanical, and biomedical properties of zirconia/hydroxyapatite ceramic composites, Ceram. Int. 48 (2022) 12376–12386, https://doi.org/10.1016/j.ceramint.2022.01.102.
[4] S. Zhong, Q. Shi, Y. Deng, Y. Sun, C. Politis, S. Yang, High-performance zirconia ceramic additively manufactured via NanoParticle Jetting, Ceram. Int. 48 (2022) 33485–33498, https://doi.org/10.1016/j.ceramint.2022.07.294.
[5] H.G. Scott, Phase relationships in the zirconia-yttria system, J. Mater. Sci. 10 (1975) 1527–1535, https://doi.org/10.1007/BF01031853.
[6] T. Yu, Z. Zhang, Q. Liu, R. Kuliiev, N. Orlovskaya, D. Wu, Extrusion-based additive manufacturing of yttria-partially-stabilized zirconia ceramics, Ceram. Int. 46 (2020) 5020–5027, https://doi.org/10.1016/j.ceramint.2019.10.245.
[7] S.P.S. Badwal, F.T. Ciacchi, V. Zelizko, The effect of alumina addition on the conductivity, microstructure and mechanical strength of zirconia - yttria electrolytes, Ionics 4 (1998) 25–32, https://doi.org/10.1007/BF02375776.
[8] F. Toldra-Reig, J.M. Serra, Surface functionalization with Ni of $Fe_{0.7}Cr_{1.3}O_3$/8YSZ electrode in a potentiometric sensor to selectively detect C_2H_4, ACS Appl. Nano Mater. 1 (2018) 6666–6673, https://doi.org/10.1021/acsanm.8b01486.
[9] L. Cross, R. Raj, S.I.A. Jalali, On the catalytic effect of zirconia on flash sintering of alumina, J. Am. Ceram. Soc. 105 (2022) 3746–3752, https://doi.org/10.1111/jace.18423.
[10] M. Borghetti, M. Serpelloni, E. Sardini, S. Pandini, Mechanical behavior of strain sensors based on PEDOT:PSS and silver nanoparticles inks deposited on polymer substrate by inkjet printing, Sensors Actuators, A Phys. 243 (2016) 71–80, https://doi.org/10.1016/j.sna.2016.03.021.

[11] F. Xu, X. Li, Y. Shi, L. Li, W. Wang, L. He, R. Liu, Recent developments for flexible pressure sensors: a review, Micromachines 9 (2018) 580, https://doi.org/10.3390/mi9110580.

[12] X. Luo, A. Morrin, A.J. Killard, M.R. Smyth, Application of nanoparticles in electrochemical sensors and biosensors, Electroanal. An Int. J. Devoted to Fundam. Pract. Asp. Electroanal. 18 (2006) 319–326, https://doi.org/10.1002/elan.200503415.

[13] Y. Gao, L. Yu, J.C. Yeo, C.T. Lim, Flexible hybrid sensors for health monitoring: materials and mechanisms to render wearability, Adv. Mater. 32 (2020), 1902133, https://doi.org/10.1002/adma.201902133.

[14] M.M.M. Carrijo, H. Lorenz, C.R. Rambo, P. Greil, N. Travitzky, Fabrication of Ti_3SiC_2-based pastes for screen printing on paper-derived Al_2O_3 substrates, Ceram. Int. 44 (2018) 8116–8124, https://doi.org/10.1016/j.ceramint.2018.01.256.

[15] W. Wu, Inorganic nanomaterials for printed electronics: a review, Nanoscale 9 (2017) 7342–7372, https://doi.org/10.1039/c7nr01604b.

[16] W.J. Hyun, S. Lim, B.Y. Ahn, J.A. Lewis, C.D. Frisbie, L.F. Francis, Screen printing of highly loaded silver inks on plastic substrates using silicon stencils, ACS Appl. Mater. Interfaces 7 (2015) 12619–12624, https://doi.org/10.1021/acsami.5b02487.

[17] J. Zhang, M. Ahmadi, G. Fargas, N. Perinka, J. Reguera, S. Lanceros-Méndez, L. Llanes, E. Jiménez-Piqué, Silver nanoparticles for conductive inks: From synthesis and ink formulation to their use in printing technologies, Metals 12 (2) (2022) 234, https://doi.org/10.3390/met12020234.

[18] J. Wang, B. Tian, V.B. Nascimento, L. Angnes, Performance of screen-printed carbon electrodes fabricated from different carbon inks, Electrochim. Acta 42 (1998) 3459–3465, https://doi.org/10.1016/S0013-4686(98)00092-9.

[19] G.B. Tseghai, B. Malengier, K.A. Fante, A.B. Nigusse, L. Van Langenhove, Development of a flex and stretchy conductive cotton fabric via flat screen printing of PEDOT:PSS/PDMS conductive polymer composite, Sensors 20 (2020) 1742, https://doi.org/10.3390/s20061742.

[20] R. Salomoni, P. Léo, A.F. Montemor, B.G. Rinaldi, M.F.A. Rodrigues, Antibacterial effect of silver nanoparticles in Pseudomonas aeruginosa, Nanotechnol. Sci. Appl. 10 (2017) 115–121, https://doi.org/10.2147/NSA.S133415.

[21] A. Pajor-Świerzy, Y. Farraj, A. Kamyshny, S. Magdassi, Air stable copper-silver core-shell submicron particles: synthesis and conductive ink formulation, Colloids Surfaces A Physicochem. Eng. Asp. 521 (2017) 272–280, https://doi.org/10.1016/j.colsurfa.2016.08.026.

[22] V. Raman, Y.H. Cho, H.M. Kim, Y.J. Kim, H.M. Sim, H.K. Kim, Ag mesh network framework based nano composite for transparent conductive functional electrodes for capacitive touch sensor and thin film heater, Ceram. Int. 47 (2021) 27230–27240, https://doi.org/10.1016/j.ceramint.2021.06.145.

[23] Q. Wu, S. Zou, F.P. Gosselin, D. Therriault, M.C. Heuzey, 3D printing of a self-healing nanocomposite for stretchable sensors, J. Mater. Chem. C 6 (2018) 12180–12186, https://doi.org/10.1039/C8TC02883D.

[24] X.Y. Yin, Y. Zhang, X. Cai, Q. Guo, J. Yang, Z.L. Wang, 3D printing of ionic conductors for high-sensitivity wearable sensors, Mater. Horiz. 6 (2019) 767–780, https://doi.org/10.1039/c8mh01398e.

[25] L. Shi, M. Layani, X. Cai, H. Zhao, S. Magdassi, M. Lan, An inkjet printed Ag electrode fabricated on plastic substrate with a chemical sintering approach for the electrochemical sensing of hydrogen peroxide, Sensor. Actuator. B Chem. 256 (2018) 938–945, https://doi.org/10.1016/j.snb.2017.10.035.

[26] X. Peng, J. Yuan, S. Shen, M. Gao, A.S.R. Chesman, H. Yin, J. Cheng, Q. Zhang, D. Angmo, Perovskite and organic solar cells fabricated by inkjet printing: progress and prospects, Adv. Funct. Mater. 27 (2017), 1703704, https://doi.org/10.1002/adfm.201703704.

[27] S.W. Leow, W. Li, J.M.R. Tan, S. Venkataraj, V. Tunuguntla, M. Zhang, S. Magdassi, L.H. Wong, Solution-processed semitransparent CZTS thin-film solar cells via cation substitution and rapid thermal annealing, Sol. RRL. 5 (2021), 2100131, https://doi.org/10.1002/solr.202100131.

[28] S. Chung, K. Cho, T. Lee, Recent progress in inkjet-printed thin-film transistors, Adv. Sci. 6 (2019), 1801445, https://doi.org/10.1002/advs.201801445.

[29] J. Sun, B. Cui, F. Chu, C. Yun, M. He, L. Li, Y. Song, Printable nanomaterials for the fabrication of high-performance supercapacitors, Nanomaterials 8 (2018) 528, https://doi.org/10.3390/nano8070528.

[30] G. Cai, P. Darmawan, M. Cui, J. Wang, J. Chen, S. Magdassi, P.S. Lee, Highly stable transparent conductive silver grid/PEDOT: PSS electrodes for integrated bifunctional flexible electrochromic supercapacitors, Adv. Energy Mater. 6 (2016), 1501882, https://doi.org/10.1002/aenm.201501882.

[31] C.G. Moura, D. Faria, O. Carvalho, R.S.F. Pereira, M.F. Cerqueira, R. M. Nascimento, F.S. Silva, Laser printing of silver-based micro-wires in ZrO_2 substrate for smart implant applications, Opt Laser. Technol. 131 (2020), 106416, https://doi.org/10.1016/j.optlastec.2020.106416.

[32] Z. Cao, Q. Gao, M. Zhou, X. Li, Q. Wang, $LaNiTiO_3$-SE-based stabilized zirconium oxide mixed potentiometric SO_2 gas sensor, Ceram. Int. 48 (2022) 9269–9276, https://doi.org/10.1016/j.ceramint.2021.12.113.

[33] H. Tian, H. Liu, H. Cheng, Microstructural and electrical properties of thick film resistors on oxide/oxide ceramic–matrix composites, Ceram. Int. 41 (2015) 3214–3219, https://doi.org/10.1016/j.ceramint.2014.10.181.

[34] B. Brandt, M. Gemeinert, T. Rabe, J. Bolte, Low-temperature co-fired ceramic substrates for high-performance strain gauges, Int. J. Appl. Ceram. Technol. 10 (2013) 413–420, https://doi.org/10.1111/ijac.12052.

[35] M. Hrovat, D. Belavič, A. Benčan, J. Holc, Evaluating the compatibility of some thick-film resistors and tetragonal zirconia, J. Mater. Sci. Lett. 20 (2001) 1605–1607, https://doi.org/10.1023/A:1017981206725.

[36] M. Hrovat, D. Belavič, A. Benčan, J. Holc, Thick-film resistors on zirconia substrates for possible strain gauge applications, J. Eur. Ceram. Soc. 23 (2003) 1441–1448, https://doi.org/10.1016/S0955-2219(02)00355-2.

[37] S. Merilampi, T. Laine-Ma, P. Ruuskanen, The characterization of electrically conductive silver ink patterns on flexible substrates, Microelectron. Reliab. 49 (2009) 782–790, https://doi.org/10.1016/j.microrel.2009.04.004.

[38] J. Zikulnig, A. Roshanghias, L. Rauter, C. Hirschl, Evaluation of the sheet resistance of inkjet-printed Ag-layers on flexible, uncoated paper substrates using van-der-pauw's method, Sensors 20 (2020) 2398, https://doi.org/10.3390/s20082398.

[39] Z. Liu, D. Qi, P. Guo, Y. Liu, B. Zhu, H. Yang, Y. Liu, B. Li, C. Zhang, J. Yu, Thickness-gradient films for high gauge factor stretchable strain sensors, Adv. Mater. 27 (2015) 6230–6237, https://doi.org/10.1002/adma.201503288.

[40] M. Wang, H. Li, Y. Li, F. Mo, Z. Li, R. Chai, H. Wang, Dispersibility and size control of silver nanoparticles with anti-algal potential based on coupling effects of polyvinylpyrrolidone and sodium tripolyphosphate, Nanomaterials 10 (2020) 1042, https://doi.org/10.3390/nano10061042.

[41] A. Rautela, J. Rani, Green synthesis of silver nanoparticles from Tectona grandis seeds extract: characterization and mechanism of antimicrobial action on different microorganisms, J. Anal. Sci. Technol. 10 (2019) 1–10, https://doi.org/10.1186/s40543-018-0163-z.

[42] P. Kanniah, J. Radhamani, P. Chelliah, N. Muthusamy, E. Joshua Jebasingh Sathiya Balasingh, J. Reeta Thangapandi, S. Balakrishnan, R. Shanmugam, Green synthesis of multifaceted silver nanoparticles using the flower extract of Aerva lanata and evaluation of its biological and environmental applications, ChemistrySelect 5 (2020) 2322–2331, https://doi.org/10.1002/slct.201903228.

[43] S. Rajeshkumar, C. Kannan, G. Annadurai, Synthesis and characterization of antimicrobial silver nanoparticles using marine brown seaweed Padina tetrastromatica, Drug Invent. Today 4 (2012) 511–513.

[44] U. Kumar Sur, B. Ankamwar, S. Karmakar, A. Halder, P. Das, Green synthesis of silver nanoparticles using the plant extract of Shikakai and Reetha, Mater. Today Proc. 5 (2018) 2321–2329, https://doi.org/10.1016/j.matpr.2017.09.236.

[45] Ľ. Hodásová, C. Alemán, L.J. Del Valle, L. Llanes, G. Fargas, E. Armelin, 3D-printed polymer-infiltrated ceramic network with biocompatible adhesive to potentiate dental implant applications, Materials 14 (2021) 5513, https://doi.org/10.3390/ma14195513.

[46] A.M. Awwad, N.M. Salem, A.O. Abdeen, Biosynthesis of silver nanoparticles using Olea europaea leaves extract and its antibacterial activity, Nanosci. Nanotechnol. 2 (2012) 164–170. https://10.5923/j.nn.20120206.03.

[47] J. Greiser, P. Müllner, E. Arzt, Abnormal growth of "giant" grains in silver thin films, Acta Mater. 49 (2001) 1041–1050, https://doi.org/10.1016/S1359-6454(00)00372-4.

[48] M.T. Rahman, J. McCloy, C.V. Ramana, R. Panat, Structure, electrical characteristics, and high-temperature stability of aerosol jet printed silver nanoparticle films, J. Appl. Phys. 120 (2016), 75305, https://doi.org/10.1063/1.4960779.

[49] E.Z. Luo, S. Heun, M. Kennedy, J. Wollschläger, M. Henzler, Surface roughness and conductivity of thin Ag films, Phys. Rev. B 49 (1994) 4858, https://doi.org/10.1103/PhysRevB.49.4858.

[50] S. Luo, L. Fan, K. Yang, Z. Zhong, X. Wu, T. Ren, In situ and controllable synthesis of Ag NPs in tannic acid-based hyperbranched waterborne polyurethanes to prepare antibacterial polyurethanes/Ag NPs composites, RSC Adv. 8 (2018) 36571–36578. https://10.1039/C8RA07575A.

[51] Z. Li, Y. Li, X.F. Qian, J. Yin, Z.K. Zhu, A simple method for selective immobilization of silver nanoparticles, Appl. Surf. Sci. 250 (2005) 109–116, https://doi.org/10.1016/j.apsusc.2004.12.039.

[52] K.S. Bhat, U.T. Nakate, J.Y. Yoo, Y. Wang, T. Mahmoudi, Y.B. Hahn, Cost-effective silver ink for printable and flexible electronics with robust mechanical performance, Chem. Eng. J. 373 (2019) 355–364, https://doi.org/10.1016/j.cej.2019.05.033.

[53] W. Yang, C. Wang, V. Arrighi, An organic silver complex conductive ink using both decomposition and self-reduction mechanisms in film formation, J. Mater. Sci. Mater. Electron. 29 (2018) 2771–2783, https://doi.org/10.1007/s10854-017-8205-7.

[54] W. Yang, C. Wang, V. Arrighi, Effects of amine types on the properties of silver oxalate ink and the associated film morphology, J. Mater. Sci. Mater. Electron. 29 (2018) 20895–20906, https://doi.org/10.1007/s10854-018-0233-4.

[55] J.K. Jadav, V.V. Umrania, K.J. Rathod, B.A. Golakiya, Development of silver/carbon screen-printed electrode for rapid determination of vitamin C from fruit juices, Lebensm. Wiss. Technol. 88 (2018) 152–158, https://doi.org/10.1016/j.lwt.2017.10.005.

[56] X. Li, B. Bhushan, Micro-nanomechanical and tribological characterization of ultrathin amorphous carbon coatings, J. Mater. Res. 14 (1999) 2328–2337, https://doi.org/10.1557/JMR.1999.0309.

[57] W.T. Hicks, T.R. Allington, V. Johnson, Membrane touch switches: thick-film materials systems and processing options, IEEE Trans. Components, Hybrids Manuf. Technol. 3 (1980) 518–524, https://doi.org/10.1109/TCHMT.1980.1135649.

[58] Y. Zhang, N. Anderson, S. Bland, S. Nutt, G. Jursich, S. Joshi, All-printed strain sensors: building blocks of the aircraft structural health monitoring system, Sensors Actuators, A Phys. 253 (2017) 165–172, https://doi.org/10.1016/j.sna.2016.10.007.

[59] E.H. Ledet, B. Liddle, K. Kradinova, S. Harper, Smart implants in orthopedic surgery, improving patient outcomes: a review, Innovat. Enterpren. Health 5 (2018) 41–51, https://doi.org/10.2147/IEH.S133518.

[60] F. Graichen, R. Arnold, A. Rohlmann, G. Bergmann, Implantable 9-channel telemetry system for in vivo load measurements with orthopedic implants, IEEE

Trans. Biomed. Eng. 54 (2007) 253–261, https://doi.org/10.1109/TBME.2006.886857.